



Universiteit
Leiden
The Netherlands

Structure of the source I disk in Orion-KL

Wright, M.; Bally, J.; Hirota, T.; Miller, K.; Harding, T.; Colletuori, K.; ... ; McGuire, B.

Citation



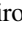




Wright, M., Bally, J., Hirota, T., Miller, K., Harding, T., Colletuori, K., ... McGuire, B. (2022).
Structure of the source I disk in Orion-KL. *The Astrophysical Journal*, 924(2).
doi:10.3847/1538-4357/ac391b

Version: Publisher's Version
License: [Creative Commons CC BY 4.0 license](https://creativecommons.org/licenses/by/4.0/)
Downloaded from: <https://hdl.handle.net/1887/3561632>

Note: To cite this publication please use the final published version (if applicable).



Structure of the Source I Disk in Orion-KL

Melvyn Wright¹ , John Bally² , Tomoya Hirota³ , Kyle Miller¹, Tyler Harding¹ , Keira Colletuori¹, Adam Ginsburg^{4,5} ,
Ciriaco Goddi⁶ , and Brett McGuire^{5,7} 

¹ Department of Astronomy, University of California, 501 Campbell Hall, Berkeley, CA 94720-3441, USA; melvyn@berkeley.edu

² CASA, University of Colorado, 389-UCB, Boulder, CO 80309, USA

³ Mizusawa VLBI Observatory, National Astronomical Observatory of Japan, Osawa 2-21-1, Mitaka, Tokyo 181-8588, Japan

⁴ Department of Astronomy, University of Florida, 211 Bryant Space Science Center P.O. Box 112055, Gainesville, FL 32611-2055, USA

⁵ National Radio Astronomy Observatory, Charlottesville, VA 22903, USA

⁶ Leiden Observatory, Leiden University, P.O. Box 9513, 2300 RA Leiden, The Netherlands

⁷ Department of Chemistry, Massachusetts Institute of Technology, Cambridge, MA 02139, USA

Received 2021 June 21; revised 2021 September 27; accepted 2021 October 20; published 2022 January 18

Abstract

This paper analyses images from 43 to 340 GHz to trace the structure of the Source I (SrcI) disk in Orion-KL with ~ 12 au resolution. The data reveal an almost edge-on disk with an outside diameter ~ 100 au, which is heated from the inside. The high opacity at 220–340 GHz hides the internal structure and presents a surface temperature ~ 500 K. Images at 43, 86 and 99 GHz reveal structure within the disk. At 43 GHz there is bright compact emission with brightness temperature ~ 1300 K. Another feature, most prominent at 99 GHz, is a warped ridge of emission. The data can be explained by a simple model with a hot inner structure, seen through cooler material. A wide-angle outflow mapped in SiO emission ablates material from the interior of the disk, and extends in a bipolar outflow over 1000 au along the rotation axis of the disk. SiO $\nu = 0$, $J = 5-4$ emission appears to have a localized footprint in the warped ridge. These observations suggest that the ridge is the working surface of the disk, and heated by accretion and the outflow. The disk structure may be evolving, with multiple accretion and outflow events. We discuss two sources of variability: (1) variable accretion onto the disk as SrcI travels through the filamentary debris from the Becklin–Neugebauer Object–SrcI encounter ~ 550 yr ago; and (2) episodic accretion from the disk onto the protostar, which may trigger multiple outflows. The warped inner-disk structure is direct evidence that SrcI could be a binary experiencing episodic accretion.

Unified Astronomy Thesaurus concepts: Protostars (1302); Circumstellar disks (235); Binary stars (154); Star formation (1569); Star forming regions (1565)

1. Introduction

The Kleinmann–Low (KL) nebula in Orion, at a distance 415 pc (Menten et al. 2007; Kim et al. 2008; Kounkel et al. 2018), is the nearest HII region in which massive ($M > 8 M_{\odot}$) stars are forming. The two most massive objects in this region, Source I (SrcI) and the Becklin–Neugebauer Object (BN), appear to be recoiling from one another at $35-40 \text{ km s}^{-1}$ (Rodríguez et al. 2005; Gómez et al. 2008; Goddi et al. 2011b), suggesting that they were ejected from a multiple system via dynamical decay approximately 550 yr ago (Bally et al. 2020). SrcI has an estimated mass of $\sim 15 M_{\odot}$ (Ginsburg et al. 2018), with a rotating accretion disk, a hot inner core obscured by a dusty outer envelope, and a molecular outflow that is prominent in shock-tracing SiO in several rotational-vibration levels.

The region around SrcI has been well studied since the 1980s (Hirota et al. 2014; Plambeck & Wright 2016); it is an active source associated with variable SiO and H₂O masers (Reid et al. 2007; Goddi et al. 2009; Plambeck et al. 2009; Matthews et al. 2010; Goddi et al. 2011b; Niederhofer et al. 2012; Greenhill et al. 2013).

The SiO emission and other properties of SrcI are reminiscent of similar features often observed in evolved stars. However, the density of asymptotic giant branch stars within ~ 1 kpc of the Sun is low, $\sim 25 \text{ kpc}^{-2}$ (e.g., Jura & Kleinmann 1989), and the chance

of one located at the center of the Orion cluster being captured and dynamically ejected in the BN–SrcI encounter is small. Although SrcI shows SiO maser emission similar to evolved stars, SiO vibrationally excited masers have been detected in several other high-mass star-forming regions (Hasegawa et al. 1986; Higuchi et al. 2015; Ginsburg et al. 2015; Cho et al. 2016; Cordiner et al. 2016; Kalenskii & Johansson 2010). The presence of a disk-outflow system (Hirota et al. 2017) indicates that SrcI is accreting, confirming its nature as a young, forming star.

In this paper, we analyze high-resolution continuum images from 43 to 340 GHz to trace the structure of the SrcI disk at ~ 30 mas (12 au) resolution.

The paper is organized as follows. Section 2 presents the observations and data reduction, Section 3 discusses the results for the SrcI disk, and Section 4 summarizes the conclusions.

2. Observations and Data Reduction

We used Karl G. Jansky Very Large Array (JVLA) and Atacama Large Millimeter/submillimeter Array (ALMA) data at 43, 86, 99, 223 and 340 GHz to make 30 mas resolution images of the continuum emission from Orion SrcI. Table 1 provides a summary of the observations, including project codes and synthesized beam FWHM with robust = -2 weighting of the UV data. The MIRIAD software package (Sault et al. 1995) was used to image and analyze all the data in this paper.

We present a new continuum image at 86 GHz using the spectral line data described in Hirota et al. (2020). The data were calibrated using observatory-supplied scripts. We used averaged



Original content from this work may be used under the terms of the [Creative Commons Attribution 4.0 licence](https://creativecommons.org/licenses/by/4.0/). Any further distribution of this work must maintain attribution to the author(s) and the title of the work, journal citation and DOI.

Table 1
Observations

Freq (GHz)	Project code	Date	Time (min)	Synth beam (milliarcsec)	Baseline (meters)
43	VLA/18A-136	2018-03-06	291	39 × 34 at PA 1	500-36600
86 and 99	2017.1.00497.S	2017-10-12	158	45 × 36 at PA 47	40-16200
224	2016.1.00165.S	2017-09-19	44	39 × 19 at PA 66	40-10500
340	2016.1.00165.S	2017-11-08	45	26 × 11 at PA 58	90-12900

spectra of the UV data to identify line-free channels to image the SrcI disk in continuum emission. The data include four spectral windows, each with 59 MHz bandwidth and 480 channels, and five spectral windows, each with 59 MHz bandwidth and 240 channels.

We averaged the line-free channels on both ends of each spectral window resulting in 18 averages of line-free UV data, with frequencies and bandwidths given in Table 2.

We imaged these 18 averages and plotted the total flux and peak from Gaussian fits versus frequency in order to verify the consistency of the continuum images. After subtracting the average continuum image, the residual images were consistent with Gaussian noise distributions. Thus, the 86 GHz continuum image is not significantly contaminated by unidentified spectral line emission.

We made images with several different weightings of the UV data: using robust = -2 weighting to produce a more uniform weighting of the UV data to emphasize compact structures, and robust = +2 weighting for better sensitivity to low-brightness, more-extended emission.

We then made a multi-frequency synthesis (MFS) image from the averaged line-free UV data. The image includes the BN source ~10" northwest from SrcI. We deconvolved the image using the CLEAN algorithm over the full field of the image, including the BN source. Sidelobes from BN could contaminate SrcI, although the full field looks clean. The image including BN also provides a flux check on SrcI, and will be presented in another paper. The MFS image of SrcI at 86 GHz is shown in Figure 1.

2.1. 43 GHz and 99 GHz

The 43 GHz and 99 GHz (ALMA Band 3; B3) observations and calibration are described in Hirota et al. (2020) and Wright et al. (2020). The 43 GHz JVLA observations included 16 wideband spectral windows each covering 116 MHz bandwidth. The wideband average with a mean frequency of 42.65 GHz and a bandwidth of 1.4 GHz excludes four spectral windows containing spectral line emission.

ALMA observations at 99 GHz included four spectral windows, each with a bandwidth of 1.875 GHz and 960 spectral channels. The wideband average with a mean frequency of 99.275 GHz and a bandwidth of 7.5 GHz excludes channels with spectral line emission.

2.2. 223 and 340 GHz

The 223 GHz (ALMA Band 6; B6) and 340 GHz (ALMA Band 7; B7) observations and calibration are described in Ginsburg et al. (2018). Images of SrcI with 30 mas resolution at 99, 220, and 340 GHz (Wright et al. 2020) are shown in Figure 2.

Table 2
86 GHz Continuum Frequencies

Spectral window	Frequency (GHz)	Frequency (GHz)	Bandwidth (MHz)
0	86.263704	86.223543	18.3
1	86.867220	86.827058	18.3
8	86.263376	86.223215	18.3
9	86.866891	86.826730	18.3
2	84.763768	84.728856	23.4
4	85.776890	85.741978	23.4
5	85.184697	85.149785	23.4
10	84.763444	84.728532	23.4
12	85.776567	85.741655	23.4

2.3. Spectral Index Distribution

We made spectral index (SI) images between 86 GHz and 43 GHz images clipped at 25 K. Figure 3 shows the SI computed from the ratio of continuum brightness at 86 and 43 GHz. SI images between 43, 99, 222, and 340 GHz are shown in Wright et al. (2020).

In Figure 3, we see that the central source is more prominent at 43 GHz, and also note the steepening of the SI at the ends of the disk between 43 and 86 GHz.

We checked the individual spectral windows at 43 and 86 GHz for any residual spectral line contamination in the averaged continuum images. After subtracting the average continuum images shown in Figure 3, the individual spectral windows are consistent with Gaussian noise distributions. Thus, the continuum and SI images are not significantly contaminated by unidentified spectral line emission.

Errors in the spectral indices are also limited by the absolute flux calibration, resulting in an accuracy of ~10% for each frequency band. A least-squares fit from 43 to 340 GHz to the SI at the central position gives $1.6 \pm .1$ whereas at the ends of the disk the fitted SI is $3.4 \pm .3$.

3. Discussion

3.1. Disk Structure

Ginsburg et al. (2018) fitted the observed structure of the disk from B3 and B6 ALMA continuum observations at 50 and 20 mas resolution, respectively. They determined that the disk has a length of ~100 au, and vertical FWHM height of ~20 au. They also detected a compact source near the center of the disk, smeared parallel to the disk major axis.

Table 3 summarizes the results of Gaussian fits to the disk size from the 43 to 340 GHz images. The disk major axis increases with observing frequency, which is expected as the dust optical depth increases. The minor axis is largest at 43 GHz, however,

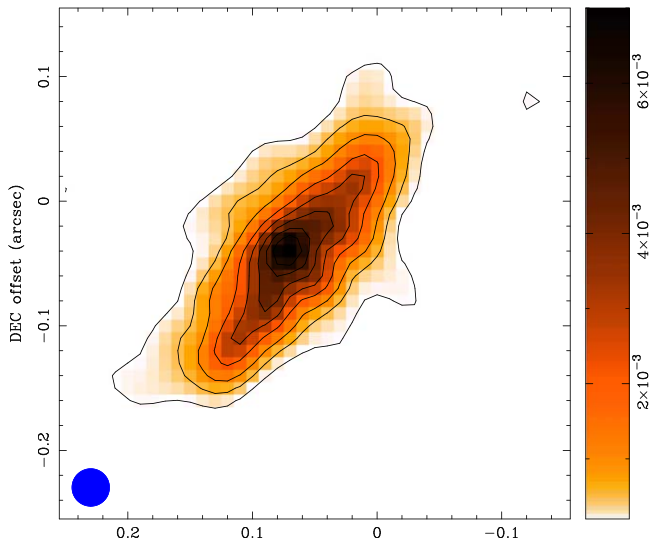


Figure 1. Source I continuum emission at 86 GHz. Contour levels: 0.2, 0.5, 1, 2, 3, 4, 5, 6, 7 mJy beam⁻¹. The 30 mas convolving beam FWHM is indicated in blue in the lower left.

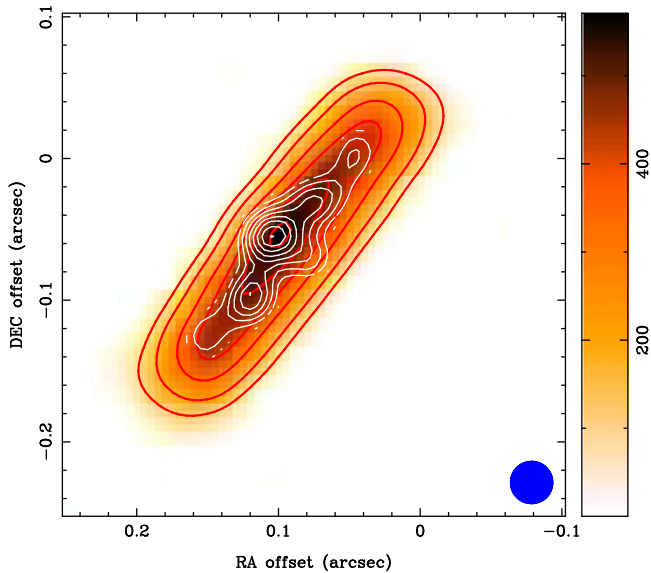


Figure 2. Source I continuum emission at 99, 220, and 340 GHz. White contour levels at 99 GHz: 50, 100, 200, 300, 400, 500, 600, 700, 800, 900, 1000 K. Red contour levels at 220 GHz: 50, 100, 200, 300, 400, 500 K. The pixel image shows the continuum emission at 340 GHz in K. The 30 mas convolving beam FWHM is indicated in blue in the lower right.

indicating that the compact source is more prominent at lower frequencies.

Figures 1, 2, 3, and 4 show images of the source structure at 30 mas resolution visible from 43 to 340 GHz. Some substructures are evident: (1) a compact source most prominent at 43 GHz; (2) a SI ~ 3 at the ends of the disk along the major axis; (3) an extended region with SI < 2 along the minor axis, and extensions along the major axis ridge; and (4) a warped ridge of emission at 43, 86, and 99 GHz—most prominent at 86 and 99 GHz, but still visible at 220 and 340 GHz.

We discuss these structures in the following section.

3.1.1. Compact Source

The peak brightness at 220 and 340 GHz coincides with the compact source seen in the 43–99 GHz images. As argued in

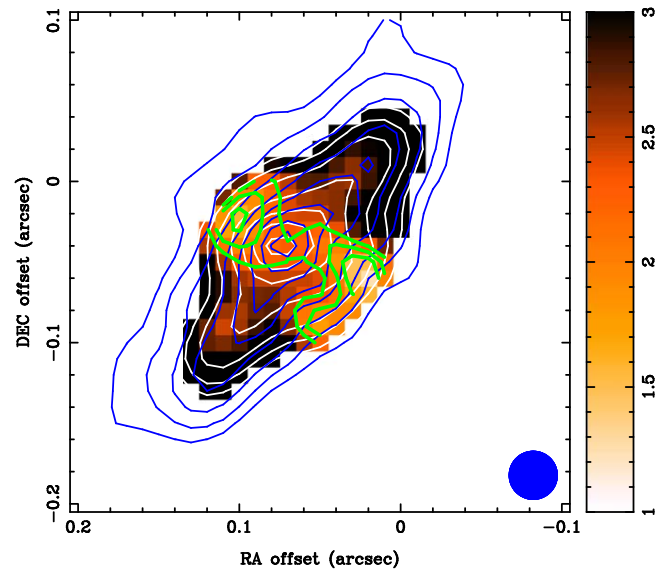


Figure 3. Spectral index (SI) 43 GHz to 86 GHz. White contour levels at 43 GHz: 50, 100, 200, 400, 600, 800, 1000, 1200 K. Blue contour levels at 86 GHz: 50, 100, 200, 400, 600, 800, 1000, 1200 K. The color image shows the SI distribution. The thick green contours at SI = 1.7, 2, and 2.3 delineate the region of lower SI along the minor axis of the disk. The 30 mas convolving beam FWHM is indicated in blue in the lower right.

Table 3
Measured Sizes and Flux Densities for Source I

Freq (GHz)	Deconvolved size (arcsec, PA)	Integrated flux (mJy)
43	$0.099 \pm 0.002 \times 0.057 \pm 0.002, -40.4^\circ \pm 2.7^\circ$	10 ± 1
86	$0.142 \pm 0.005 \times 0.044 \pm 0.001, -38.0^\circ \pm 1.0^\circ$	48 ± 5
99	$0.151 \pm 0.005 \times 0.044 \pm 0.002, -37.8^\circ \pm 1.3^\circ$	58 ± 6
224	$0.197 \pm 0.003 \times 0.042 \pm 0.003, -37.3^\circ \pm 0.4^\circ$	256 ± 25
340	$0.234 \pm 0.005 \times 0.042 \pm 0.002, -37.4^\circ \pm 0.3^\circ$	630 ± 63

Ginsburg et al. (2018), the position is offset from the center of the disk, and the source is extended, suggesting that it is a hot region in the inner disk, and not the location of the central source powering SrcI.

3.2. Spectral Index

The SI images in Wright et al. (2020) also show a SI ~ 3 at the ends of the disk associated with dust emission, and the region with SI < 2 along the minor axis of the disk. Our new image at 86 GHz shows an extended region with SI < 2 along the minor axis, as well as a narrow region tracing the warped ridge which is evident in the 99 GHz and 86 GHz continuum images. We discuss three mechanisms which could produce an SI < 2 .

3.2.1. Free-free Emission and Ionized Jets

Plambeck & Wright (2016) analyzed the continuum flux densities measured for SrcI from 4 to 690 GHz. Above 43 GHz the flux density is consistent with emission from optically thick dust. At lower frequencies, the flux densities are higher than the ν^2 fit, and free-free emission may become important where the dust emission becomes optically thin (see Plambeck & Wright 2016).

The H26 α (353.6 GHz) and H21 α (662.4 GHz) hydrogen recombination lines were not detected. Plambeck & Wright (2016)

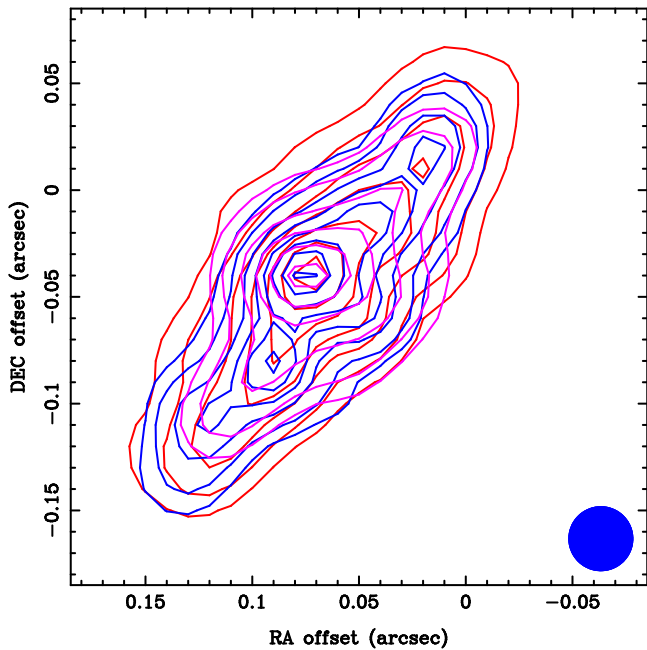


Figure 4. 43 GHz, 86 GHz, and 99 GHz structure. Purple contour levels at 43 GHz: 100, 200, 400, 600, 800, 1000, 1200 K. Red contour levels at 86 GHz: 100, 200, 400, 600, 800, 1000, 1200 K. Blue contour levels at 99 GHz: 100, 200, 400, 600, 800, 1000, 1200 K. The 30 mas convolving beam FWHM is indicated in blue in the lower right.

used a velocity range $5 < \text{VLSR} < 23 \text{ km s}^{-1}$ to establish upper limits on the intensities of the recombination lines. The blueshifted portion of the recombination lines would be confused by an unidentified emission line at 353.648 GHz, and a strong absorption by a transition of SO_2 at 662.4043 GHz (see Plambeck & Wright 2016, Figure 6). The data were integrated in a $0''.2 \times 0''.2$ box centered on SrcI. No recombination lines were detected in the SrcI disk with an upper limit 5% of the total continuum flux. Electron-neutral free-free emission (Reid et al. 2007) may be responsible for the higher flux densities below 43 GHz. An ionized jet would have a $\text{SI} < 2$. Although no well-collimated jet has been detected in SrcI, the extensions to the northeast along the minor axis at 43 GHz, and a smaller one at 86 GHz (see Figure 7) have a $\text{SI} \sim 1$. Recent radio continuum surveys have detected a number of high-mass young stellar objects (YSOs) associated with radio jets (Purser et al. 2016). They are thought to be driven from closer to the central YSOs given their higher velocities of a few 100 km s^{-1} . Similar to these other high-mass YSOs, there could be a compact radio jet in SrcI emanating from the inner region. In NGC7538 IRS1, for example, Sandell et al. (2020) find that the size of the core decreases as $\nu^{-0.92}$, with a $\text{SI} \alpha = 0.87$ (see Sandell et al. 2020, Figure 2), which is consistent with an ionized jet (Reynolds 1986). High-resolution observations at longer wavelengths are required to determine if SrcI harbors an ionized jet. The data do not preclude a small contribution to the continuum from free-free emission, but this would not account for the extended regions we see with $\text{SI} < 2$.

3.2.2. Nonthermal Emission

Nonthermal emission may contribute to the observed SI of the SrcI disk. Synchrotron emission is known to develop in the circumstellar disk jets of massive protostars (Araudo et al. 2021). Sanna et al. (2019) detected a nonthermal jet at 8 GHz, which is driven by a young massive star in the star-forming region G035.02+0.35.

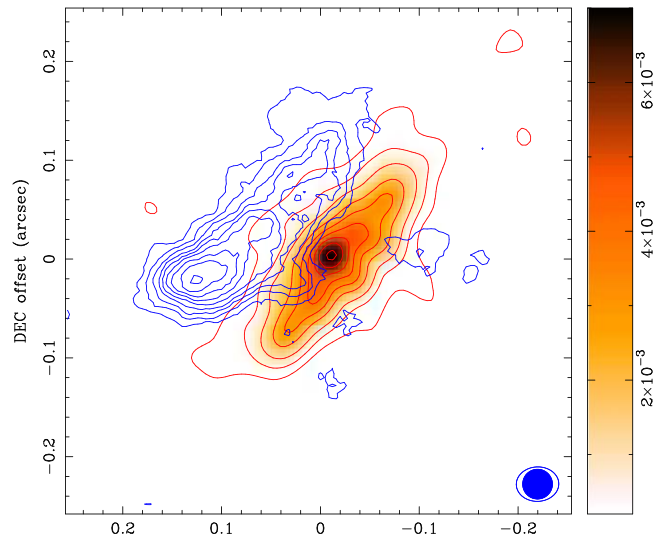


Figure 5. AIO $N = 6-5$ emission at 229.6938725 GHz overlaid on 86 GHz continuum emission. Red contours show the 86 GHz continuum emission at 37 to 1280 K with a contour interval of 183 K. Blue contours show the AIO $N = 6-5$ emission integrated over -50 to 50 km s^{-1} . Lowest contour and contour interval 500 K km s^{-1} . The 30 mas convolving beam FWHM for the 86 GHz continuum image is indicated by the blue filled circle. The FWHM beam for the AIO $N = 6-5$ is 0.04×0.03 arcsec in PA -88° , and is shown as the open ellipse in the lower right.

However, this mechanism is unlikely in SrcI because a well-formed jet is not observed. Synchrotron emission is associated with $\text{SI} < 1$, and might also be observed close to the surface of the star, but not in the extended circumstellar disk as observed in SrcI. Hirota et al. (2020) did not find any polarization in the SrcI disk, which might also be expected for synchrotron emission.

3.2.3. Dust Opacity

A simple explanation could be a temperature gradient in the disk which reveals hotter material in the inner disk at lower frequencies where the opacity in the disk is lower. A hot inner disk is also suggested by the observations of high-excitation SiO transitions (Ginsburg et al. 2019, see Figure 5; Kim et al. 2019; Hirota et al. 2017), and H_2O emission (Wright et al. 2020).

Figure 5 shows contours of the AIO $N = 6-5$ emission integrated over -50 to 50 km s^{-1} , overlaid on the 86 GHz continuum emission. The AIO emission forms a cone on the northeast side of the disk, with a wide-angle outflow extending from the warped ridge in the 86 GHz continuum emission from the SrcI disk. The distributions of AIO emission shown here are consistent with those presented by Tachibana et al. (2019) for AIO $N = 13-12$ and $N = 17-16$ emission lines at 497 and 650 GHz, who suggest that AIO is formed at the base of the outflow, and condenses further out into the outflow. Our observations with $\sim 4\times$ higher angular resolution show that AIO emission extends from deep within the SrcI disk, and may be produced by grain destruction. Lenzuni et al. (1995) investigated the evaporation of dust grains in protostellar cores. Carbon grains are destroyed at temperatures $\sim 800-1150 \text{ K}$. Silicate grains are evaporated at temperatures $\sim 1300 \text{ K}$, and AIO at $\sim 1700 \text{ K}$. The distribution of AIO offers strong support for ablation of the disk into a hollowed-out cone, leaving a flared disk of cooler material that obscures the interior, with high dust opacity at higher frequencies. The strongly asymmetric distribution of AIO emission suggests that the heating

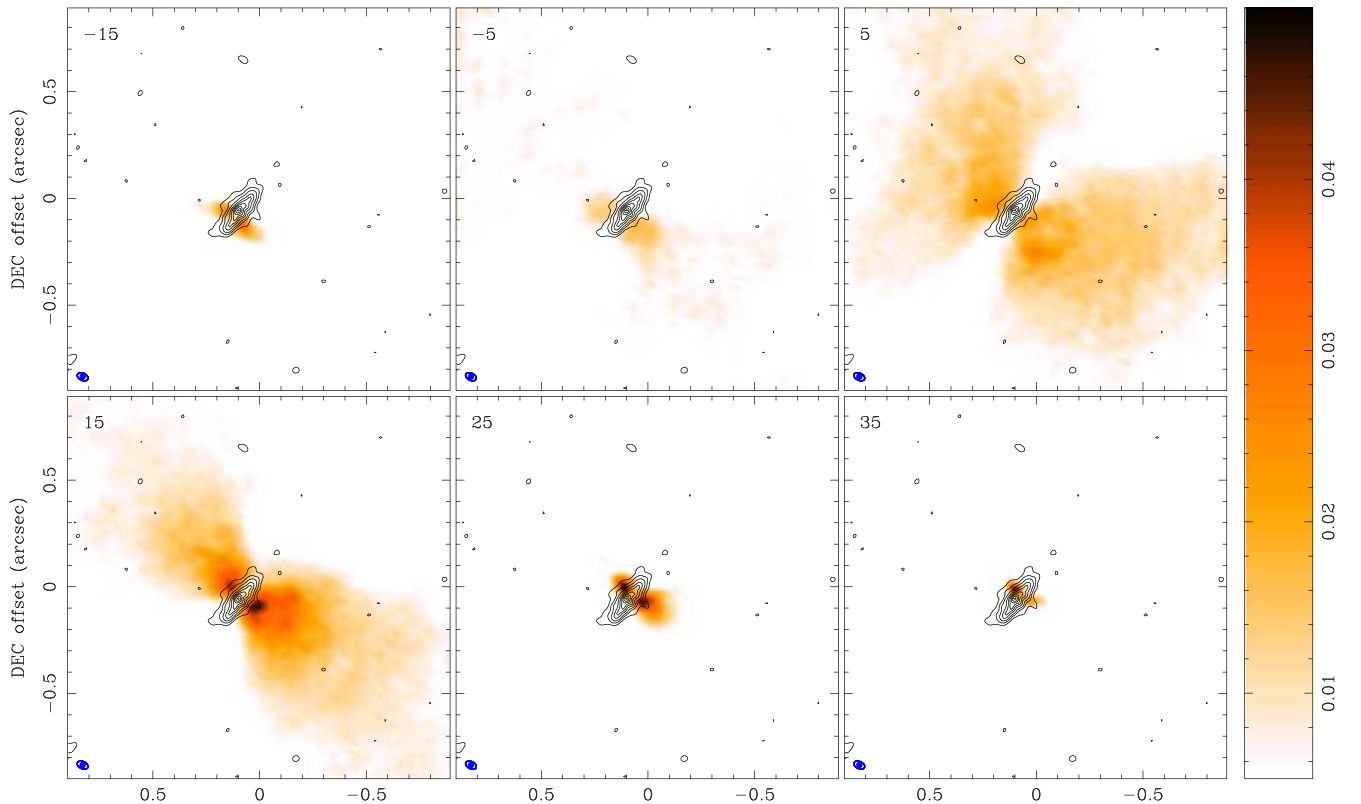


Figure 6. SiO $\nu = 0$, $J = 5-4$ emission at 217.10498 GHz overlaid on 86 GHz continuum. The color image shows the high-velocity SiO $\nu = 0$, $J = 5-4$ emission at 10 km s^{-1} intervals. Beam FWHM $54 \times 34 \text{ mas}$ in PA 65° . Red contours show the 86 GHz continuum image. Contours at .2, .5, 1, 2, 3, 4, 5, 6, 7 mJy/beam in a 30 mas FWHM beam (37, 91, 183, 366, 549, 732, 915, 1097, 1280 K).

source is associated with the compact source seen at 43 GHz on the east side of the disk.

The inner surface must be $\sim 1700 \text{ K}$ to evaporate AIO. The outer surface temperature of the disk is observed to be $\sim 500 \text{ K}$ at higher frequencies. Radiation from the structure of the interior of the SrcI disk is absorbed in the exterior part of the disk.

Although the heating of the disk may be complex, the temperature of the disk material can be quite well described by a simple radiative transfer model with a hot inner surface of the disk and a cool outer surface, in which the radiation from the inner surface is attenuated by the disk.

We fitted a simple model with a hot inner surface layer of a cavity (excavated by the outflow and luminosity of SrcI) with brightness temperature, T_{in} , and an outer surface with brightness temperature, T_{out} . Radiation from the inner surface is attenuated by the disk. We assume an opacity which scales as ν^β :

$$T_{\text{obs}}(\nu) = T_{\text{in}}(\nu)(\exp(-\tau_{\nu_0}(\nu/\nu_0)^\beta) + T_{\text{out}}(\nu). \quad (1)$$

We searched a parameter space of T_{in} , T_{out} , $\tau_{43\text{GHz}}$, and β toward the compact source for our observations at 43, 86, 99, 220, and 340 GHz. At 30 mas resolution, minimum Chisq fits to the observed brightness temperature T_{obs} were in the range $T_{\text{in}} = 1000-1500 \text{ K}$, $T_{\text{out}} = 400-600 \text{ K}$, $\tau_{43\text{GHz}} = 0.1-0.75$, and $\beta = 0.75-2$, with the range of values corresponding to a doubling of Chisq around the minimum. At other positions away from the compact source, which is offset from the center of the disk, the model requires further assumptions about the geometry and heating of the disk. The inner surface may be heated by radiation from SrcI, shocks from the outflow and

accreting material, and radiative heating from the outer surface and outflow. With 30 mas (12 au) resolution, the observed brightness, T_{obs} , averages over several features seen in the SrcI disk, and the interpretation is less clear away from the compact source. Observations with better resolution and sensitivity would enable more detailed modeling.

Our crude two-temperature model is inspired by a similar model used in Li et al. 2017, and fits the hypothesis that the SI is dominated at low frequencies by the H^- opacity and at higher frequencies by the cool-dust opacity obscuring the inner disk. The implied luminosity at the inner and outer surfaces with these temperatures are consistent with the luminosity of SrcI $\sim 10,000 L_\odot$. Modeling the disk as a cylinder with radius 50 au and length 21 au (see Table 3), the luminosity for a blackbody with a surface temperature in the range 400–600 K is $\sim 2000-9500 L_\odot$. For the inner surface, using a radius $\sim 40 \text{ au}$, defined by the AIO emission, with a surface temperature in the range 1000–1500 K, the luminosity is $\sim 1600-8300 L_\odot$.

The nearly edge-on disk is opaque at IR and submillimeter wavelengths (e.g., at 340 and 220 GHz), but at 43–90 GHz the internal structure of the disk is revealed. Radiation at IR wavelengths can escape into the wide-angle outflow, and may contribute to the excitation of the SiO maser emission (Goddi et al. 2009), and salt emission (Ginsburg et al. 2019).

3.2.4. The Warped Ridge

The nature of the warped ridge of emission which is observed from 43 to 99 GHz is not clear. The ridge is most prominent at 99 GHz, and manifests only as an extended peak in the brightness distributions at 220 and 340 GHz, as shown in

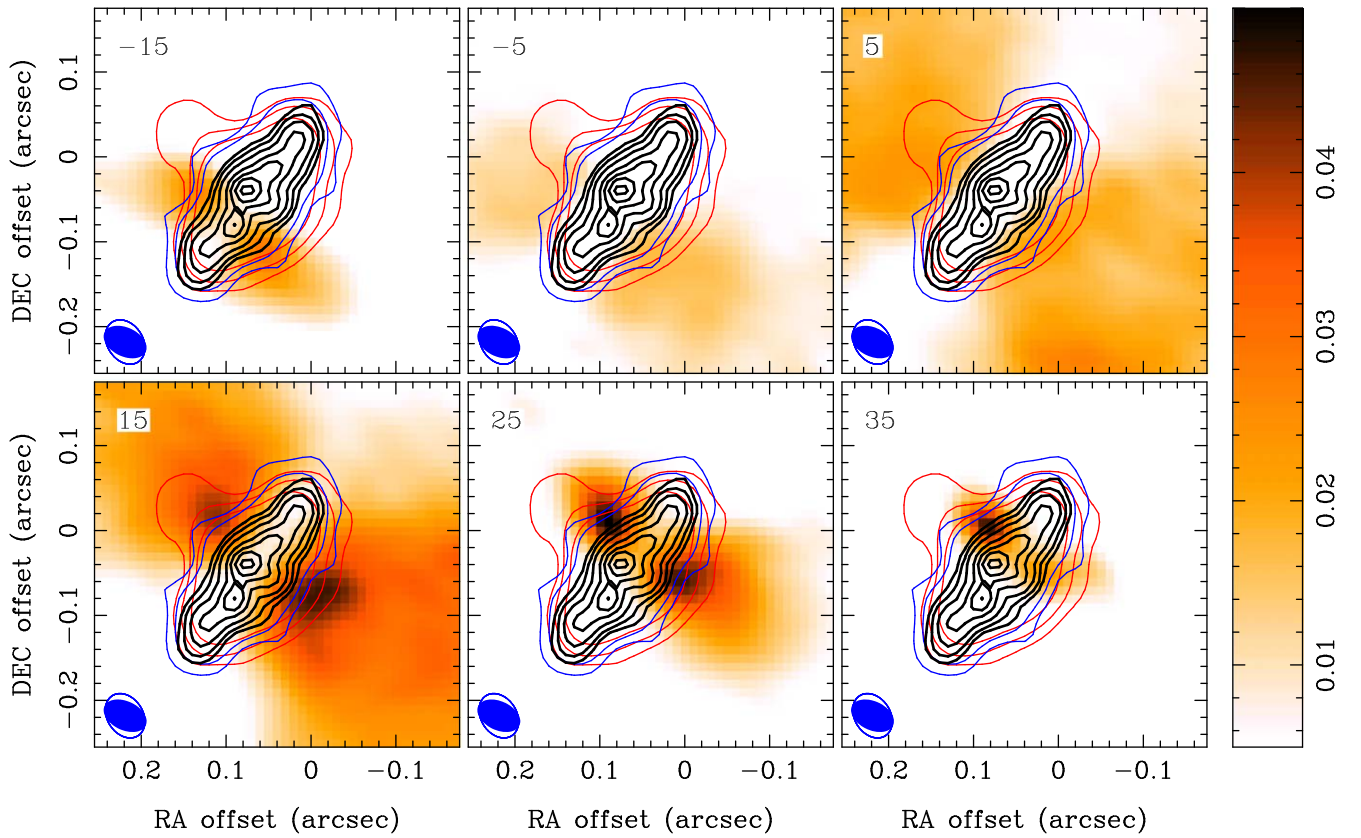


Figure 7. SiO $\nu = 0$, $J = 5-4$ emission at 217.10498 GHz overlaid on contours of the 99, 86, and 43 GHz continuum emission. The thick black contours at 99 GHz at 50, 100, 200, 300, 400, 500, 600, 700, 800, 900, 1000 K with a 30 mas FWHM show the inner structure in the disk. The blue contours at 86 GHz at 50 and 100K, and the red contours at 43 GHz at 25, 50, and 100K are convolved to 56×42 mas FWHM resolution to show the structure at the edge of the disk. The color image shows SiO $\nu = 0$, $J = 5-4$ emission at 10 km s^{-1} intervals. Beam FWHM 54×34 mas in PA 65° . The beams are shown in the lower left.

Figure 2 and Figure 4. These observations suggest emission from the hot inner parts of the disk, which is absorbed at 220 and 340 GHz by cooler material in the outer disk. The ridge could represent a warped disk structure, or filaments which are accreting onto SrcI. Such observable asymmetries are expected in the inner regions of circumbinary disks (Avramenko et al. 2017). Assuming an enclosed mass $15 M_\odot$, the period of orbit is 15 yr for material at 15 au radius and 90 yr at 50 au. The encounter with BN ~ 500 yr ago is sufficient time to wind up remains of filaments which may have been accreting onto SrcI before the encounter. However, the twisted ridge may trace active accretion in SrcI.

Figure 6 shows SiO $\nu = 0$, $J = 5-4$ emission at 217.10498 GHz overlaid on the 86 GHz continuum emission. The SiO $J = 5-4$ line shows emission at velocities outside the range -10 to $+20 \text{ km s}^{-1}$ seen in the $J = 1-0$ and $J = 2-1$ lines (Hirota et al. 2020). This high-velocity SiO emission extends from close to the mid-plane of the disk, between the cusps of low-brightness continuum in the 86 GHz emission at the outer edge of the disk. The outflow is closest to the center at $\sim -20 \text{ km s}^{-1}$, and $+30 \text{ km s}^{-1}$. If we assume that the outflow is attached to the rotation of the disk, then we can estimate the inner radius, $r_{\text{inner}} = GM/v^2 \sim 20$ au from the footprint of the SiO $J = 5-4$ emission. This radius is consistent with the launching radius for a magneto-centrifugal wind determined from the rotation of the SiO $\nu = 0$, $J = 5-4$ outflow (see Equation (4) in Anderson et al. 2003), and consistent with that determined by Hirota et al. (2017).

In order to investigate the relationship of the SiO emission to the continuum emission in more detail, we deconvolved the 99 GHz image using the CLEAN algorithm. The CLEAN models are not unique, but when convolved by the synthesized beam are consistent with the synthesized image, and a residual image with a Gaussian distribution of pixel values with an rms noise level 0.4 mJy. Images of the four spectral windows which were used to make the 99 GHz continuum image are consistent. As a further check, we made CLEAN models using an alternative self-calibration based on an SiO $\nu = 1$ maser feature, instead of the standard calibration. Both images show the twisted ridge of emission.

Figure 7 shows SiO $\nu = 0$, $J = 5-4$ emission overlaid on the 99, 86, and 43 GHz continuum emission. The 99 GHz emission is convolved to a 30 mas resolution to show the inner structure in the disk. The blue contours at 86 GHz at 50 and 100K, and red contours at 43 GHz at 25, 50, and 100K, are convolved to 56×42 mas FWHM resolution to show the structure at the edge of the disk. The high-velocity SiO emission appears quite localized, with a clear footprint in the twisted ridge observed in the continuum emission, whereas the SiO emission between -10 and $+20 \text{ km s}^{-1}$ stands away from the continuum ridge. At the edge of the disk, the high-velocity SiO emission emerges in the cusps of the outer contours at 86 and 43 GHz, suggesting that material is ablated by the outflow. These observations suggest that the twisted ridge traces the working surface of the disk, which is heated by accretion onto the disk and the disruption of the disk surface by the outflow.

3.3. Spectral Energy Distribution

There is another potential connection to the twisted ridge not yet mentioned. As highlighted above, the optical depth increases with frequency and the twisted ridge structure appears clearest around $\sim 86\text{--}99$ GHz. The question remains if the structure evident in the images is directly related to apparent curvature on wideband spectral energy distributions (SEDs) (Plambeck & Wright 2016; Beuther et al. 2006); it is possible that a noncollisional mechanism is exciting the SiO $J=5\text{--}4$ outflow and is related to both the excess flux density at low frequencies, which Plambeck & Wright (2016) attributed to free-free emission (probably H⁺ free-free emission), and the warped ridge. A full analysis of the SED is beyond the scope of this paper.

3.4. Disk Mass, Accretion, and Outflow

In this section we discuss accretion and outflow in the disk. The circumbinary disk might have an evolving structure with variable accretion and outflows. The disk mass is estimated to be in the range $0.02\text{--}0.2 M_{\odot}$ (Plambeck & Wright 2016). A disk mass of $\sim 0.1 M_{\odot}$ was derived in Hirota et al. (2017). Any original disk would have been truncated to the observed radius in the encounter between SrcI and BN (Moeckel & Goddi 2012; Ginsburg et al. 2018; Bally et al. 2020). SrcI was ejected and is moving through the debris of the explosion at a velocity $\sim 10 \text{ km s}^{-1}$. Using a velocity $\sim 10 \text{ km s}^{-1}$ relative to the OMC-1 core, the accretion onto the disk from the ambient cloud would be limited to roughly the Bondi-Hoyle (B-H) rate, which for $n_{\text{H}_2} = 1 \times 10^7 \text{ cm}^{-3}$, $\rho \sim 3 \times 10^{-17} \text{ g cm}^{-3}$, $M = 15 M_{\odot}$, and $v = 10 \text{ km s}^{-1}$:

$$\dot{M} = \lambda_* 4\pi\rho \frac{(GM)^2}{(v^2 + c_s^2)^{3/2}} \approx 3 \times 10^{-5} M_{\odot} \text{ yr}^{-1}, \quad (2)$$

where $c_s = \sqrt{k_B T / \mu m_p}$ is the ambient thermal (sound) speed, which is in the range $1\text{--}5 \text{ km s}^{-1}$ for $T = 10\text{--}1000 \text{ K}$, and $\mu = 2\text{--}3$ with λ_* being a dimensionless constant of order unity (Shu 1991).

Considering that SrcI does not appear to be in the densest part of OMC-1, this may be an upper bound. Accretion from the filamentary debris of the BN/SrcI explosion could produce large variations in the accretion rate. SrcI may pass through multiple filaments of explosion debris at different relative velocities. For comoving material the B-H accretion rate could be as high as $3 \times 10^{-3} M_{\odot} \text{ yr}^{-1}$, assuming a sound speed $\sim 2 \text{ km s}^{-1}$. Accretion variations are to be expected as SrcI passes through the filamentary debris of the BN/SrcI explosion. The crossing time for a $1''$ (400 au) filament at 10 km s^{-1} is $\sim 200 \text{ yr}$.

Wright et al. (1995) estimated the mass of the outflow from images of the SiO $J=2\text{--}1$, $v=0$ line. Using a solar abundance of Si, $n(\text{SiO})/n(\text{H}_2) = 6 \times 10^{-5}$, the total mass in the outflow was estimated to be $\sim 5 \times 10^{-3} M_{\odot}$. Using an outflow velocity 18 km s^{-1} , the mass-loss rate is $\sim 10^{-5} M_{\odot} \text{ yr}^{-1}$ and the kinetic luminosity is $\sim 1 L_{\odot}$. Since the Si abundance and degree of masing in the SiO $J=2\text{--}1$, $v=0$ line is unknown, this is only a rough estimate. Greenhill et al. (2013), estimate a loss rate $\sim 5 \times 10^{-6} M_{\odot} \text{ yr}^{-1}$ from the SiO $J=1\text{--}0$, $v=0$ outflow.

López-Vázquez et al. (2020) derive an outflow mass from the ^{29}SiO $J=8\text{--}7$, $v=0$ line. Using an SiO abundance $1.2\text{--}2.4 \times 10^{-7}$ relative to H_2 (Ziurys & Friberg 1987), they estimate the mass of the molecular outflow $0.66\text{--}1.3 M_{\odot}$, and a

kinematic age 130 yr . This implies a mass-loss rate in the outflow $\sim 5\text{--}10 \times 10^{-3} M_{\odot} \text{ yr}^{-1}$. López-Vázquez et al. (2020) note that this estimate leads to some problems:

(i) the outflow depletes disk mass unless the accretion rate is high; and

(ii) the accretion luminosity exceeds $10^4 L_{\odot}$ if the accreting material falls onto the stars.

Ziurys & Friberg (1987) determined a SiO abundance $1.2\text{--}2.4 \times 10^{-7}$ relative to H_2 from a $\text{N}(\text{H}_2)$ column density $1\text{--}2 \times 10^{24} \text{ cm}^{-2}$, and $\text{N}(\text{SiO}) 2 \times 10^{17} \text{ cm}^{-2}$ for a $10''$ region centered on SrcI. However, the explosion 550 yr ago could have vaporized all dust.

SiO is abundant in the debris from the explosion (see Figure 17 in Wright et al. 2020). The solar abundance of Si is $\sim 3 \times 10^{-5}$ relative to H. It is possible that most Si ended up in SiO. If so, the H_2 mass in the SrcI outflow could be much lower than López-Vázquez et al. (2020) estimate. This would lower the mass-loss rate estimate correspondingly. But, if the mass estimate ($\sim 1 M_{\odot}$) and timescale ($\sim 130 \text{ yr}$) stand, then there must be a better explanation.

Episodic accretion is a possibility. The SiO $v=0$, $J=5\text{--}4$ images in Figure 6 suggest different outflow events for the bright compact, high-velocity emission, and the more-extended emission between -10 to $+20 \text{ km s}^{-1}$. The different extents of the SiO $v=0$, $J=5\text{--}4$ emission could have resulted from different outflow events. Shocks from multiple outflow events may also be responsible for the abrupt change in the SiO $v=0$, $J=2\text{--}1$ emission outflows from a rotating column into a wide-angle outflow $\sim 50 \text{ au}$ from the SrcI disk (see Figures 1 and 2 in Hirota et al. 2020). Another possible interpretation of the collimated and wide-angle outflows are different driving mechanisms at different launching regions (Machida 2014; Matsushita et al. 2017).

There is direct evidence from IR photometry and the morphology of the outflows that mass-loss rate, and therefore accretion, is highly variable. Bally et al. (2020) argued that these parameters likely follow a “ $1/f$ ” distribution: small variations on short timescales and very large variations on long timescales.

The mJy H_2O maser flare in Orion (Matveenko et al. 1982) appears to mark a spot in the southwest portion of the SrcI outflow. It may trace a shock where fast ejecta ran into slower-moving material. Thus, it might be an indirect indicator of mass-loss-rate and/or velocity variability.

If the inflow rate in the disk is $0.01 M_{\odot} \text{ yr}^{-1}$, why is the luminosity only $L \sim 10^4 L_{\odot}$?

Perhaps the accretion merely transfers gas from a larger radius to a smaller one without landing on the central star or binary. The inflow might be prevented from falling onto the central object, perhaps by magnetic stress or a centrifugal barrier if the disk wind is not sufficiently efficient in removing angular momentum.

Alternatively, if the central object is accreting at a very high rate ($> 1 \times 10^{-3} M_{\odot} \text{ yr}^{-1}$), a $15 M_{\odot}$ protostar will have an au-scale photosphere (e.g., Hosokawa & Omukai 2009). Accretion at a rate of $0.01 M_{\odot} \text{ yr}^{-1}$ onto a $15 M_{\odot}$ object with an $R \sim 1 \text{ au}$ photosphere would have a luminosity of $\sim 2 \times 10^4 L_{\odot}$. This is *not* inconsistent with the $T_{\text{eff}} \sim 4000 \text{ K}$ photospheric temperature found by Testi et al. (2010) from the SrcI IR reflection nebulosity.

If the central object is a merger remnant, left over from the dynamical interaction 550 yr ago, its photosphere may be

especially bloated because it takes a Kelvin–Helmholtz time-scale time to radiate away the energy liberated by a collision between two stars.

3.5. Evidence for a Binary in SrcI

The warped inner-disk structure may be direct evidence that SrcI is a binary. A possible explanation for our observations is an unequal binary that is experiencing episodic accretion. Dunhill et al. (2015) describe numerical simulations of the circumbinary disk around the young, eccentric stellar binary HD 104237. They find that the binary clears out a large cavity in the disk, driving a significant eccentricity at the cavity edge. The disk precesses around the binary, which for HD 104237 corresponds to a precession period of 40 yr. The accretion from the disk onto the binary changes with this precession, resulting in a periodic accretion variability determined by the parameters of the binary and its orbit. They find an order of magnitude changes in the accretion rate onto the binary.

Dunhill et al. (2015) give the disk precession period as $360/0.48 \times T_{\text{binary}} = 40$ yr for HD 104237. $T_{\text{binary}} = \sqrt{\frac{R^3}{M}}$, where R is in au and M is in M_{\odot} . The favored scenario for the formation of the binary in the BN/SrcI explosion gives an orbital separation 1–9 au, with an average of 4 au in the last 50 yr of the simulation (Goddi et al. 2011a). For $R = 1$ au, 2 au, and 4 au, and using a mass of $15 M_{\odot}$, the precession periods are ~ 194 yr, ~ 578 yr, and ~ 1549 yr, respectively. Although we do not see any evidence of precession in the SiO outflow in the last 500 yr, the faster precession would be relevant to the idea of episodic accretion. From extensive N -body simulations Goddi et al. (2011a) and Moeckel & Goddi (2012) concluded that the dynamical history of BN/KL cannot be reconstructed with unequal-mass binaries. Goddi et al. (2011a) considered N -body simulations with up to 11 stars and masses in the range 0.5 – $10 M_{\odot}$. In order to have a $10 M_{\odot}$ star ejected (BN), the binary must have been comprised of the largest stars in the sample ($10+10 M_{\odot}$). Moeckel & Goddi (2012) investigated the disk survival in the presence of a stellar encounter between a binary and intruder. In the case of an unequal-mass binary $10+3 M_{\odot}$, stellar ejections were possible only by swapping the $3 M_{\odot}$ binary member with the $10 M_{\odot}$ intruder, resulting in a $10+10 M_{\odot}$ binary, but there was no case with a $10+3 M_{\odot}$ binary and $10 M_{\odot}$ runaway. However, an accretion event, after the compact binary ejection, which initiates an SiO outflow is not excluded from these simulations. Farias & Tan (2018) made $\sim 10^7$ N -body simulations including binary–binary interactions. They conclude that the BN/SrcI requires a SrcI mass $\sim 20 M_{\odot}$, but note that other possible initial combinations remain to be explored.

Ragusa et al. (2020) studied the evolution of coplanar binaries and the circumbinary discs, using three-dimensional smoothed particle hydrodynamics simulations. They find that, even with circular initial conditions, all discs with mass ratios $q > 0.05$ develop eccentricity, and that the disk eccentricity grows abruptly after ~ 400 – 700 binary orbits, and is associated with a very small increase in the binary eccentricity.

Goddi et al. (2020) present evidence for episodic accretion from the structure of the SiO jet in W51-North, where different SiO outflow axes on different scales are likely a consequence of episodic accretion, like an FU Orionis event, but for higher masses. It would be interesting if we see possible evidence of episodic events in SrcI. As suggested by Hirota et al. (2014),

the super maser flare could have a periodicity of 13 yr (1985, 1998, 2011), although there was no confirmed flare event in 1973. In order to confirm the periodicity, we are waiting for the next flare. Even if there is no regular periodicity, it could suggest time-variable star formation activities either in SrcI or unknown YSO in the Compact Ridge (Hirota et al. 2014).

Based on these models, the compact source that we observe at 43 GHz could be the current site of accretion from the disk onto the binary, and driving the most recent outflows. An unequal binary could provide episodic accretion, as well as provide a possible explanation for the warped ridge of emission.

The thick green contours at $SI = 1.7, 2,$ and 2.3 in Figure 3 delineate the region of lower SI along the minor axis of the disk. The twist in the SI contours is in the direction of disk rotation, suggesting that material ablated from the disk is caught up in the disk rotation. The twist has a footprint close to the compact source in the warped ridge, and extends to the edge of the disk with a twist < 1 turn. The 43 GHz and 86 GHz observations were obtained within a ~ 5 month period (see Table 1), so the offset in the images from the proper motion of SrcI is less than ~ 1 au. For an outflow velocity $\sim 18 \text{ km s}^{-1}$, the time for material to reach the edge of the disk is ~ 5 yr (18 au and 18 km s^{-1} are both measured along the line of sight). Assuming an enclosed mass $15 M_{\odot}$, the period of orbit is 15 yr for material at 15 au radius, and only 3 yr at 5 au. In this case, we might expect to see changes in the structure of the disk within a few years. Future observations could reveal changes in the structure of the outflows or disk in SrcI. A more accurate determination of accretion events would also allow us to set constraints on the binary parameters. A warped disk is expected in the presence of a central binary, and this could be direct evidence that SrcI is a binary. The formation of tight binaries through decay of nonhierarchical multiple systems is a clear mechanism for evolution from wide-separation to close-separation binaries within star-forming regions, which may help solve the problem of a lack of short-period binary systems in early-stage, high-mass star-forming regions (Sana et al. 2017).

4. Summary

1. We present a new image of the SrcI disk at 86 GHz with ~ 30 mas resolution.
2. Images at 43, 86 99, 220, and 340 GHz reveal significant structure in the SrcI disk: a compact source most prominent at 43 GHz, and a warped ridge of emission at 86 and 99 GHz. The warped inner-disk structure may be evidence for a non-axis-symmetric potential within the disk, or recent accretion events.
3. The spectral index is $SI \sim 3$ at the ends of the disk along the major axis, and there is an extended region with $SI < 2$ along the minor axis, and along the major axis ridge.
4. The observed SI of the disk can be understood as a hot inner core and cool, dusty outer envelope first discussed in Ginsburg et al. (2018).
5. We fitted a simple model with hot inner structure heated by SrcI, with brightness temperature T_{in} , and an cooler outer surface with brightness temperature T_{out} . Radiation from the inner structure is attenuated by the outer disk. Assuming an opacity which scales as ν^{β} , the best fits to the observed brightness temperature toward the compact source for our observations at 43, 86, 99, 220, and 340 GHz at 30 mas resolution are in the range $T_{\text{in}} = 1000$ – 1500 K, $T_{\text{out}} =$

400–600 K, $\tau_{43\text{ GHz}} = 0.1\text{--}0.75$, and $\beta = 0.75\text{--}2$. The warped ridge is consistent with emission from the hot inner parts of the disk, which is absorbed at 220 and 340 GHz by cooler material in the outer disk.

6. High-velocity SiO $v = 0$, $J = 5\text{--}4$ emission has a footprint in the warped ridge. We suggest that the ridge traces the working surface on the disk which is heated by accretion onto the binary and the disruption of the inner disk surface by the outflow.

7. The disk structure may be evolving, with multiple accretion and outflow events. We identify two sources of variability: variable accretion onto the circumbinary disk as SrCl travels through the filamentary debris from the BN-SrCl encounter ~ 550 yr ago; and episodic accretion from the circumbinary disk onto the binary, which may trigger multiple outflows.

We thank Gibor Basri, Richard Plambeck and Goran Sandell for insightful discussions, which have improved this paper. We thank the referee for a careful reading, which has improved the presentation of this paper. This paper makes use of ALMA data listed in Table 1. ADS/JAO.ALMA#2016.1.00165.S, ADS/JAO.ALMA#2017.1.00497.S. ALMA is a partnership of ESO (representing its member states), NSF (USA) and NINS (Japan), together with NRC (Canada), MOST and ASIAA (Taiwan), and KASI (Republic of Korea), in cooperation with the Republic of Chile. The Joint ALMA Observatory is operated by ESO, AUI/NRAO, and NAOJ.

The National Radio Astronomy Observatory is a facility of the National Science Foundation operated under cooperative agreement by Associated Universities, Inc. T.H. is financially supported by the MEXT/JSPS KAKENHI grant Nos. 17K05398, 18H05222, and 20H05845.


Facilities: ALMA, VLA.

Software: Miriad (Sault et al. 1995).

ORCID iDs

Melvyn Wright  <https://orcid.org/0000-0002-9154-2440>

John Bally  <https://orcid.org/0000-0001-8135-6612>

Tomoya Hirota  <https://orcid.org/0000-0003-1659-095X>

Tyler Harding  <https://orcid.org/0000-0002-1324-8094>

Adam Ginsburg  <https://orcid.org/0000-0001-6431-9633>

Ciriaco Goddi  <https://orcid.org/0000-0002-2542-7743>

Brett McGuire  <https://orcid.org/0000-0003-1254-4817>

References

- Anderson, J. M., Li, Z.-Y., Krasnopolsky, R., & Blandford, R. D. 2003, *ApJL*, **590**, L107
- Araudo, A., Padovani, M., & Marcowith, A. 2021, *MNRAS*, **504**, 2405
- Avramenko, R., Wolf, S., & Illenseer, T. F. 2017, *A&A*, **604**, A38
- Bally, J., Ginsburg, A., Forbrich, J., & Vargas-González, J. 2020, *ApJ*, **889**, 178
- Beuther, H., Zhang, Q., Reid, M. J., et al. 2006, *ApJ*, **636**, 323
- Cho, S.-H., Yun, Y., Kim, J., et al. 2016, *ApJ*, **826**, 157
- Cordiner, M. A., Boogert, A. C. A., Charnley, S. B., et al. 2016, *ApJ*, **828**, 51
- Dunhill, A. C., Cuadra, J., & Dougados, C. 2015, *MNRAS*, **448**, 3545
- Farias, J. P., & Tan, J. C. 2018, *A&A*, **612**, L7
- Ginsburg, A., Bally, J., Goddi, C., Plambeck, R., & Wright, M. 2018, *ApJ*, **860**, 119
- Ginsburg, A., McGuire, B., Plambeck, R., et al. 2019, *ApJ*, **872**, 54
- Ginsburg, A., Walsh, A., Henkel, C., et al. 2015, *A&A*, **584**, L7
- Goddi, C., Ginsburg, A., Maud, L. T., Zhang, Q., & Zapata, L. A. 2020, *ApJ*, **905**, 25
- Goddi, C., Greenhill, L. J., Chandler, C. J., et al. 2009, *ApJ*, **698**, 1165
- Goddi, C., Greenhill, L. J., Humphreys, E. M. L., Chandler, C. J., & Matthews, L. D. 2011a, *ApJL*, **739**, L13
- Goddi, C., Humphreys, E. M. L., Greenhill, L. J., Chandler, C. J., & Matthews, L. D. 2011b, *ApJ*, **728**, 15
- Gómez, L., Rodríguez, L. F., Loinard, L., et al. 2008, *ApJ*, **685**, 333
- Greenhill, L. J., Goddi, C., Chandler, C. J., Matthews, L. D., & Humphreys, E. M. L. 2013, *ApJL*, **770**, L32
- Hasegawa, T., Morita, K., Okumura, S., et al. 1986, in *Masers, Molecules, and Mass Outflows in Star Formation Regions*, ed. A. D. Haschick (Westford, MA: Haystack Observatory), 275
- Higuchi, A. E., Hasegawa, T., Saigo, K., Sanhueza, P., & Chibueze, J. O. 2015, *ApJ*, **815**, 106
- Hirota, T., Kim, M. K., Kurono, Y., & Honma, M. 2014, *ApJL*, **782**, L28
- Hirota, T., Machida, M. N., Matsushita, Y., et al. 2017, *NatAs*, **1**, 0146
- Hirota, T., Plambeck, R. L., Wright, M. C. H., et al. 2020, *ApJ*, **896**, 157
- Hosokawa, T., & Omukai, K. 2009, *ApJ*, **691**, 823
- Jura, M., & Kleinmann, S. G. 1989, *ApJ*, **341**, 359
- Kalenskii, S. V., & Johansson, L. E. B. 2010, *ARep*, **54**, 295
- Kim, M. K., Hirota, T., Machida, M. N., et al. 2019, *ApJ*, **872**, 64
- Kim, M. K., Hirota, T., Honma, M., et al. 2008, *PASJ*, **60**, 991
- Kounkel, M., Covey, K., Suárez, G., et al. 2018, *AJ*, **156**, 84
- Lenzuni, P., Gail, H.-P., & Henning, T. 1995, *ApJ*, **447**, 848
- Li, J. I.-H., Liu, H. B., Hasegawa, Y., & Hirano, N. 2017, *ApJ*, **840**, 72
- López-Vázquez, J. A., Zapata, L. A., Lizano, S., & Cantó, J. 2020, *ApJ*, **904**, 158
- Machida, M. N. 2014, *ApJL*, **796**, L17
- Matsushita, Y., Machida, M. N., Sakurai, Y., & Hosokawa, T. 2017, *MNRAS*, **470**, 1026
- Matthews, L. D., Greenhill, L. J., Goddi, C., et al. 2010, *ApJ*, **708**, 80
- Matveenko, L. I., Moran, D. M., & Genzel, R. 1982, *SvAL*, **8**, 382
- Menten, K. M., Reid, M. J., Forbrich, J., & Brunthaler, A. 2007, *A&A*, **474**, 515
- Moeckel, N., & Goddi, C. 2012, *MNRAS*, **419**, 1390
- Niederhofer, F., Humphreys, E. M. L., & Goddi, C. 2012, *A&A*, **548**, A69
- Plambeck, R. L., & Wright, M. C. H. 2016, *ApJ*, **833**, 219
- Plambeck, R. L., Wright, M. C. H., Friedel, D. N., et al. 2009, *ApJL*, **704**, L25
- Purser, S. J. D., Lumsden, S. L., Hoare, M. G., et al. 2016, *MNRAS*, **460**, 1039
- Ragusa, E., Alexander, R., Calcino, J., Hirsh, K., & Price, D. J. 2020, *MNRAS*, **499**, 3362
- Reid, M. J., Menten, K. M., Greenhill, L. J., & Chandler, C. J. 2007, *ApJ*, **664**, 950
- Reynolds, S. P. 1986, *ApJ*, **304**, 713
- Rodríguez, L. F., Poveda, A., Lizano, S., & Allen, C. 2005, *ApJL*, **627**, L65
- Sana, H., Ramírez-Tannus, M. C., de Koter, A., et al. 2017, *A&A*, **599**, L9
- Sandell, G., Wright, M., Güsten, R., et al. 2020, *ApJ*, **904**, 139
- Sanna, A., Moscadelli, L., Goddi, C., et al. 2019, *A&A*, **623**, L3
- Sault, R. J., Teuben, P. J., & Wright, M. C. H. 1995, in *ASP Conf. Ser. 77, A Retrospective View of MIRIAD*, ed. R. A. Shaw, H. E. Payne, & J. J. E. Hayes (San Francisco, CA: ASP), 433
- Shu, F. 1991, *The Physics of Astrophysics: Gas Dynamics*, Series of Books in Astronomy (Mill Valley, CA: Univ. Science Books), <https://books.google.com/books?id=50VYSc56URUC>
- Tachibana, S., Kamizuka, T., Hirota, T., et al. 2019, *ApJL*, **875**, L29
- Testi, L., Tan, J. C., & Palla, F. 2010, *A&A*, **522**, A44
- Wright, M., Plambeck, R., Hirota, T., et al. 2020, *ApJ*, **889**, 155
- Wright, M. C. H., Plambeck, R. L., Mundy, L. G., & Looney, L. W. 1995, *ApJL*, **455**, L185
- Ziurys, L. M., & Friberg, P. 1987, *ApJL*, **314**, L49